



Stable tetravalent Ni species generated by reconstruction of FeB-wrapped NiMoO pre-catalysts enable efficient water oxidation at large current densities

Yijie Zhang^a, Kamran Dastafkan^b, Qiang Zhao^a, Jinping Li^{a,*}, Chuan Zhao^{b,*}, Guang Liu^{a,*}

^a Shanxi Key Laboratory of Gas Energy Efficient and Clean Utilization, College of Chemical Engineering and Technology, Taiyuan University of Technology, Taiyuan, Shanxi 030024, PR China

^b School of Chemistry, The University of New South Wales, Sydney, NSW 2052, Australia

ARTICLE INFO

Keywords:

Water splitting
Tetravalent Ni species
Lattice oxygen mechanism
High current densities
Oxygen evolution reaction

ABSTRACT

High valence transition metals offer highly active electrocatalytic sites for oxygen evolution reaction (OER) but suffer from high formation energy and are thermodynamically unstable in the resting state. Herein, we report the generation of NiFeOOH with highly oxidized and stable tetravalent Ni species through reconstruction and electronic structure modulation. The resulted NiFeOOH electrocatalyst catalyzes OER with ultralow overpotentials of 166 and 213 mV at 10 and 100 mA cm⁻², respectively, and high stability (> 100 h) at an ultrahigh current density of 1000 mA cm⁻². The formation of stable tetravalent Ni species in NiFeOOH nanosheets/rods structure results in higher Ni-O covalency and enhanced the reactivity of lattice oxygen, thus transferring the reaction path and reducing the reaction energy barrier for OER. This work paves the way for the rational design of electrocatalysts with high-valence metal species and activated lattice oxygen for stable water oxidation at large current densities.

1. Introduction

Electrochemical water splitting is an efficient technology to convert the intermittent energy from renewable sources (e.g. solar and wind power) to hydrogen, which is a green energy carrier to achieve the carbon neutrality [1–5]. Recently, non-noble transition metal (TM)-based materials have attracted widespread attention for the electrolysis of alkaline water including oxides, hydroxides, phosphides, borides, and chalcogenides [6,7]. Nevertheless, the lack of highly active and stable active sites, especially in industry-related conditions like high current densities, limits their industrial applications. Recent experimental and theoretical studies show that high-valence TM ions can achieve a high activity for oxygen evolution reactions (OER) [8,9] by offering greater TM-O covalency to decrease the charge transfer energy (Δ) owing to a downshifted of lower Hubbard band (LHB) as well as contractive orbitals [10–12]. With the decrease in Δ and enlarged U (energy difference between upper Hubbard band (UHB) and LHB), the electronic band can be modulated to allow LHB to penetrate the O 2p band, favoring the direct coupling of oxygen orbitals to form O–O species via the lattice oxygen mechanism (LOM) [10–12]. This pathway

avoids the intrinsic scaling limitations in the traditional adsorbate evolution mechanism (AEM), thereby lowering the limiting energy barrier [12–14]. However, the formation of high valence TM ions (e.g., Ni⁴⁺ and Co⁴⁺) is usually thermodynamically unfavorable and the related phase is unstable in the resting state, as highlighted by their potential-pH Pourbaix diagrams [8,15,16]. Currently, designing OER catalysts with highly oxidized and stable TM species remains a grand challenge.

It has been established that TM-based electrocatalysts can reconstruct into (oxy)hydroxides and exhibit an enhanced OER activity during OER process [17]. For instance, F incorporation into LNFO electrocatalyst facilitates the surface reconstruction, leading to a lower overpotential of 292 mV to reach 10 mA cm⁻² [18]. Another study by Fan et al. demonstrated that *in situ* sulfur doping induces a higher degree of surface reconstruction in NiFe LDH nanosheets, resulting in an activated electrocatalyst with an overpotential of 259 mV at 100 mA cm⁻² [19]. Liu et al. discovered that FeCo(H₃O)(PO₄)₂ can undergo irreversible deep self-reconstruction, leading to the formation of Fe_{0.5}Co_{0.5}OOH, which only requires 229 mV to drive 10 mA cm⁻² [20]. In this context, multi-metallic structures typically outperform mono-metallic catalysts

* Corresponding authors.

E-mail addresses: jpli211@hotmail.com (J. Li), chuan.zhao@unsw.edu.au (C. Zhao), liuguang@tyut.edu.cn (G. Liu).

<https://doi.org/10.1016/j.apcatb.2023.123297>

Received 7 May 2023; Received in revised form 26 August 2023; Accepted 14 September 2023

Available online 16 September 2023

0926-3373/© 2023 Elsevier B.V. All rights reserved.

due to electronic structure modulation [8,21]. For instance, Fe component is reported to promote the formation of Ni^{4+} species, because Fe^{3+} is one of the strongest Lewis acid metals [11,22]. Besides intrinsic activity, the extrinsic features such as the catalyst morphology also play critical roles in facilitating the efficient release of bubbles and mass transport at high current densities [23–26]. We recently show that hydrated nickel molybdate (denoted as NiMoO) can rapidly and deeply reconstruct into the active phase $\gamma\text{-NiOOH}$ while the high aspect ratio rod-like structure aids in the efficient release of bubbles and promotes effective mass transport [27]. This inspires us to design highly oxidized Ni species with suitable nanostructures by deep reconstruction process and electronic structure and morphology engineering.

Herein, we show a FeB-wrapped NiMoO pre-catalyst and the formation of NiFeOOH nanosheets/rods structure with stable tetravalent Ni species through an *in situ* reconstruction strategy. The introduction of metalloid boron (B) induces the formation of nanosheets/rods structure due to B oxidation and leaching during the reconstruction process. Operando electrochemical, Raman, XPS and XAS characterisation reveal that the generation of Fe-O-Ni bonds promotes the surface deprotonation to induce the formation of stable Ni^{4+} and active oxygen species, which enhances the Ni-O covalency and triggers the lattice oxygen activation supported by differential electrochemical mass spectrometry (DEMS) and DFT simulation. This work presents the first example of achieving stable high-valence Ni phase through the *in situ* reconstruction strategy for realizing efficient and stable oxygen evolution at large current densities, to the best of our knowledge.

2. Experimental section

2.1. Preparation of NiOOH and NiFeOOH catalysts

NiOOH and NiFeOOH catalysts were obtained by the cyclic voltammetry (CV) scanning in a standard three-electrode electrochemical cell. The electrolyte used was a 1 M KOH solution, and the experiments were conducted at 25 °C. This process allowed the formation of NiOOH and NiFeOOH catalysts on the working electrode, which was initially composed of NiMoO or NiMoO/FeB (with a surface area of 1 cm^2).

2.2. Materials characterizations

SEM and TEM were examined by Hitachi SU8010 and JEOL 2010FEF. XRD was determined by a Bruker D8 Advance. Raman spectra were collected on InVia 1WU072 with a 532 nm excitation laser and ICP-OES was determined by Agilent 5110. The surface wettability of samples was studied by KRUS (DSA100). XPS was performed using a Thermo VG ESCALAB250. XAS measurements were investigated on an Easy XES150 system (Easy XAFS LLC, USA). DEMS measurements were carried out using a QAS 100 device (Linglu Instruments, Shanghai).

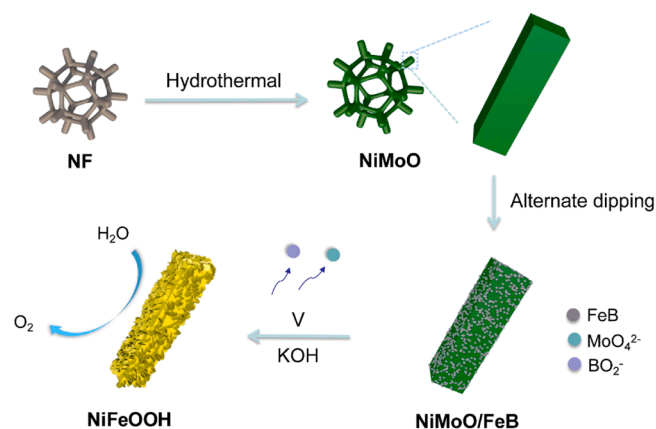
2.3. Electrochemical measurements

All electrochemical measurements were conducted in a standard three-electrode system in a 1 M KOH solution ($\text{pH} = 13.6$) at room temperature. The as-prepared electrode (working surface area: 1 cm^2), Hg/HgO (1 M KOH), and graphite rod were served as the working electrode, reference electrode, and counter electrode, respectively. The measured potentials were converted to the potentials *versus* reversible hydrogen electrode (RHE) using $E_{\text{RHE}} = E_{\text{Hg/HgO}} + 0.098 + 0.059 \times \text{pH}$. Details of the experimental section are provided in Supporting information.

3. Results and discussion

3.1. Synthesis and physical characterizations

The NiMoO/FeB pre-catalyst was prepared by a two-step routine



Scheme 1. Schematic illustration for the synthesis of NiMoO/FeB pre-catalyst and NiFeOOH catalyst.

(Scheme 1). Firstly, NiMoO rods were deposited on Ni foam (NF) via hydrothermal method, and then FeB was introduced on NiMoO surface by rapid alternating dipping method. It is worth noting that the NF not only acts as a three-dimensional conductive substrate to facilitate the release of bubbles, but also acts as a Ni source to participate in the reaction so that it is tightly coupled to prevent falling off under high current densities. Scanning electron microscopy (SEM) demonstrates smooth NiMoO microrods with a high aspect ratio uniformly coated on the surface of NF (Fig. S1). After dipping deposition, SEM and transmission electron microscopy (TEM) images reveal that the surface of the NiMoO microrods was covered by FeB nanoparticles, which were aggregated from ultrathin nanosheets (Fig. 1a-b and Fig. S2). X-ray diffraction (XRD) pattern and Raman shifts of the NiMoO/FeB are completely consistent with those of NiMoO, which are ascribed to hydrated NiMoO_4 ($\text{NiMoO}_4 \cdot 0.75\text{H}_2\text{O}$) [28–31]. While no other peaks are corresponded to the outer layer FeB nanoparticles, indicating that it is amorphous (Fig. S3). High-resolution TEM (HRTEM) images and the corresponding FFT patterns of NiMoO/FeB indicate that the inner micro-rods correspond to a monocrystalline hydrate NiMoO_4 and the outer nanoparticles are amorphous (Fig. 1c), in agreement with XRD and Raman analyses. Furthermore, scanning transmission electron microscopy (STEM) and the corresponding element mapping indicate the Ni, Mo, O, Fe and B elements are uniformly dispersed (Fig. 1d). The electronic structure of NiMoO/FeB was further studied by X-ray photoelectron spectroscopy (XPS). As displayed in Fig. S4, Ni is present as Ni^{2+} species with $2p_{3/2}$ and $2p_{1/2}$ peaks at 856.11 and 873.84 eV. The Mo 3d XPS spectrum displays two peaks with $\Delta E = 3.15\text{ eV}$, indicating that Mo is present as Mo^{6+} [32]. Fe 2p spectrum displays the coexistence of B-Fe (706.5 eV) and Fe^{3+} (712.4 eV) [33,34]. The O 1s spectrum is deconvoluted into three peaks at 530.29, 531.39 and 532.53 eV, corresponding to M-O, B-O and adsorbed H_2O , respectively. Besides, two peaks are observed for B 1s spectrum, the peak at 187.76 eV is assigned B-Fe and the peak at 191.78 eV is ascribed to metaborate (BO_2) species due to the surface oxidation (Fig. 1e) [35–37].

The NiFeOOH catalyst was obtained *via in situ* activating the NiMoO/FeB pre-catalyst during cyclic voltammetry (CV) scanning (Scheme 1 and Fig. S5). As depicted in Fig. 2a, XPS spectra indicate that Mo and B leaching induces the complete reconstruction of NiMoO/FeB. Raman and XRD analyses further confirm the complete reconstruction of NiMoO/FeB into NiFeOOH structure. The Raman and diffraction peaks of the hydrated NiMoO_4 phase completely disappear (Fig. 2b and Fig. S6). While two characteristic Raman signals at 475 and 555 cm^{-1} are detected belonging to the bending and stretching vibration modes of $\text{Ni}^{\text{III}}\text{-O}$ ($\delta(\text{Ni-O})$ and $\nu(\text{Ni-O})$), and the peaks around 678 and 1054 cm^{-1} are ascribed to Fe-O and MO-O bonds (Fig. 2b) [33,38–40].

Meanwhile, SEM (Fig. 2c and Fig. S7) and TEM (Fig. 2d) images show that the morphology transforms from nanoparticles/rods to a unique 3D

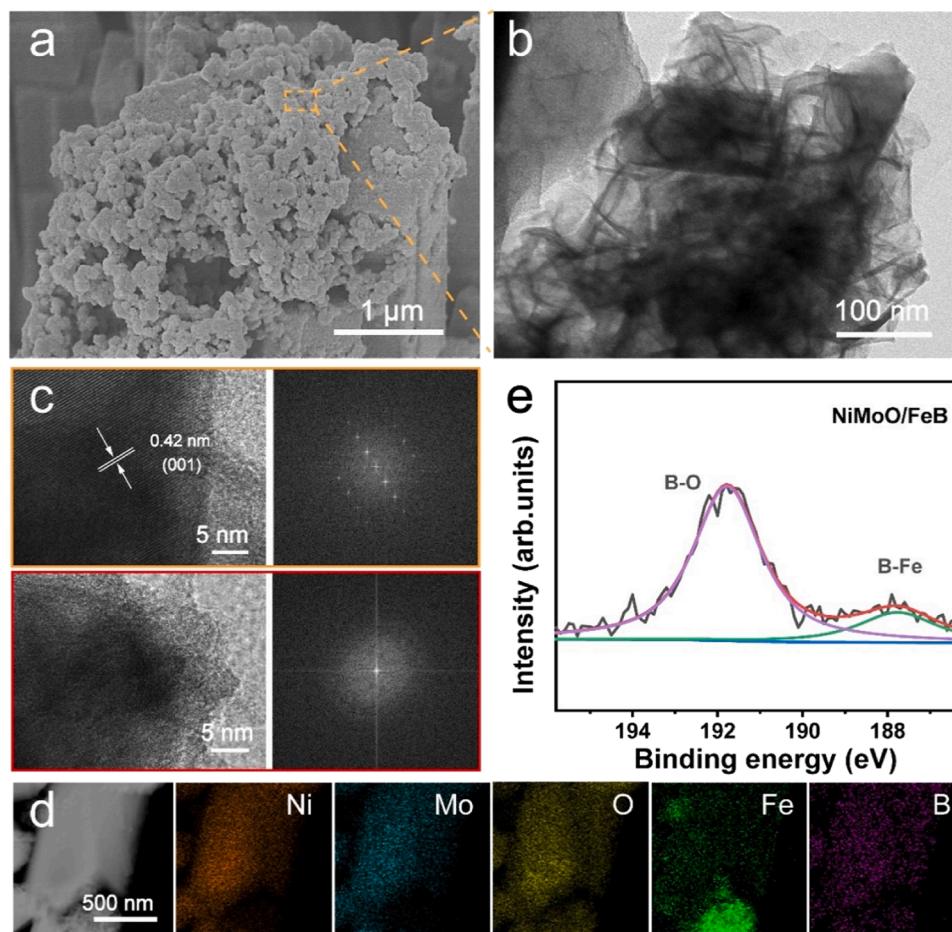


Fig. 1. (a) SEM image of NiMoO/FeB; (b) TEM image of the outer FeB. (c) HRTEM images and the corresponding FFT patterns of inner NiMoO (top) and outer FeB (bottom). (d) STEM image and the corresponding element mappings of NiMoO/FeB. (e) B 1s XPS spectrum of NiMoO/FeB.

structure consisting of nanosheets/rods after reconstruction, which is conducive for the transfer of mass and electrons [41,42], favoring efficient and stable water oxidation at high current densities. It is important to note that this transformation was caused by the disaggregation of FeB nanosheets due to B leaching during reconstruction process [36,43]. Furthermore, weak crystal lattice fringes are detected in the corresponding HRTEM image of NiFeOOH with interplanar spacings of 0.209, 0.219 and 0.237 nm matching to (105), (104) and (102) faces of NiOOH (PDF#06-0075) (Fig. 2e). Combined with the selected region electron diffraction (SAED) pattern (Fig. 2f), NiOOH exists in a low/poly-crystalline structure with abundant grain boundaries. The corresponding EDS mapping illustrates that Ni, Fe, and O are still evenly distributed in the overall structure (Fig. 2g). Nevertheless, B and Mo are almost completely leached out during reconstruction process. In addition, inductively coupled plasma-optical emission spectroscopy (ICP-OES) verified that the leaching of Mo and B and generation of trace Fe-doped (1.29%) NiOOH in the reconstruction process for NiMoO/FeB pre-catalyst (Table S1-S2). It is worth noting that the nanorods become significantly thinner after electrochemical reconstruction (Fig. 1d and Fig. 2g), and the trace amount of Ni (0.02 ppm) dissolved in the solution indicates that TM ions migration is involved in the reconstruction process (Table S2). To reveal the role of surface FeB, low/poly-crystalline NiOOH was also obtained through the reconstruction of pure NiMoO under the same conditions (Fig. S8). The absence of nanosheet structure in NiOOH demonstrates that the incorporation of B in pre-catalysts highly influences the morphology of the reconstructed catalysts. In addition, further analysis of the aerophobic property by bubbles contact angle measurement (Fig. S9), revealed a bubble contact angle of 145.6°

for NiFeOOH, which is more than NiOOH (143.1°) and NF (131.1°), indicating that the evolved bubbles were easily released attributed to the unique nanosheets/rods structure.

3.2. OER Performance

The OER activity was investigated by reverse sweep linear sweep voltammetry (LSV) in 1 M O₂-saturated KOH electrolyte to avoid the influence of metal oxidation peak before OER [40,44]. And the solution impedance was obtained by electrochemical impedance spectroscopy (EIS) test for manual iR compensation (Table S3). The influence of different dipping duration and the number of cycles were explored, where a dipping duration of 10 s and performing 2 cycles are shown to prefer the best OER performance (Fig. S10). Fig. 3a clearly demonstrates the remarkable OER activity of NiFeOOH. It exhibits an overpotential of only 166 mV, which is significantly lower compared to other materials such as NiOOH (175 mV), RuO₂ (252 mV), and bare NF (404 mV) at 10 mA cm⁻². Notably, NiFeOOH depicts a stable performance at large current densities of 500 and 1000 mA cm⁻² with low overpotentials of 277 and 315 mV, respectively, significantly better than NiOOH (Fig. 3b). In addition, we have prepared NiFeOOH without Mo and B, NiFeOOH without B, and NiFeOOH with NiFe foam substrate (Fig. S11). It can be concluded that the NF substrate has little effect on catalyst performance and Mo and B are crucial factor in the preparation of highly active NiFeOOH. Compared with NiOOH (68.8 mV dec⁻¹), RuO₂ (108.1 mV dec⁻¹) and NF (207.7 mV dec⁻¹), NiFeOOH also demonstrates a much smaller Tafel slope of 57.4 mV dec⁻¹, suggesting its superior kinetics (Fig. 3c).

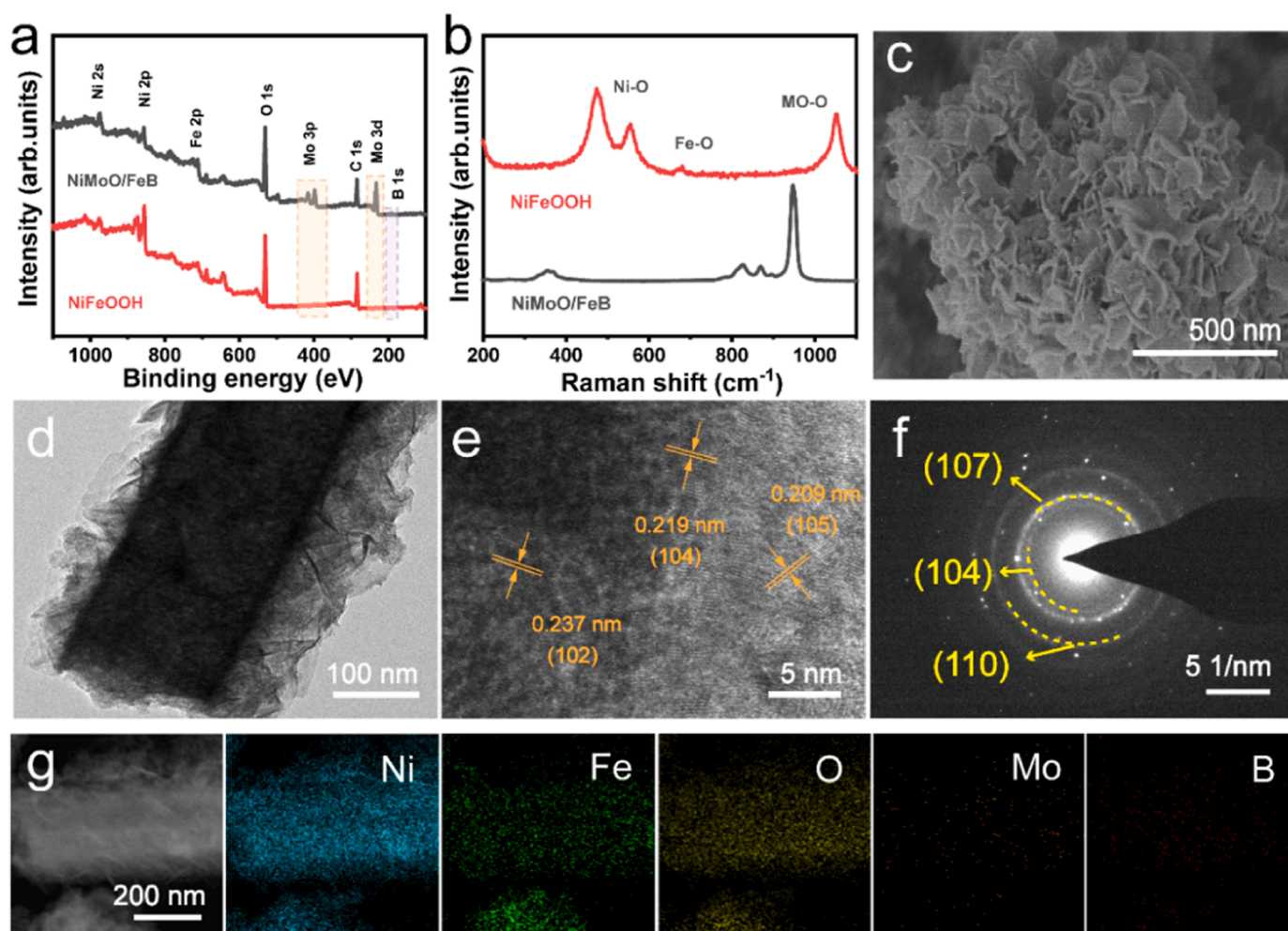


Fig. 2. (a) XPS survey spectra and (b) Raman spectra of NiMoO/FeB and NiFeOOH. (c) SEM, (d) TEM, (e) HRTEM, (f) SAED and (g) STEM images and the corresponding element mappings of NiFeOOH.

Further, the double-layer capacitance (C_{dl}) is determined by conducting CV scans at different scan rates in a non-Faradaic region, which is directly related to the electrochemical surface area (ECSA) (Fig. S12, Fig. S13a). NiFeOOH has a higher C_{dl} value than NiOOH, indicating that ECSA is enhanced due to the presence of nanosheets/rods structure. Besides, the normalized OER current densities by ECSA show a superior intrinsic activity for NiFeOOH (Fig. S13b). As illustrated in Fig. 3d, both the turnover frequency (TOF) of Ni active sites (Fig. S14) and ECSA of NiFeOOH are higher than that of NiOOH at 1.50 V vs. RHE, manifesting that the incorporation of Fe and B on the surface of NiMoO pre-catalyst effectively improve exposed active sites and intrinsic activity of the reconstructed catalyst. Notably, the developed NiFeOOH catalyst demonstrates superior performance compared to most recently reported OER electrocatalysts (Fig. 3e and Table S4) [11,23,33,45,46].

Besides, NiFeOOH also exhibits brilliant durability and stability. As indicated in Fig. S15a, NiFeOOH can drive a large current density of 1000 mA cm⁻² at 1.545 V vs. RHE for more than 100 h, with the potential increasing only by 15 mV at the end of the stability test (Fig. S15b). It is noteworthy that the nanosheets on the surface of the nanorods partially disappear under large current densities due to bubble shock and strong corrosion, while the electronic structure of the NiFeOOH is virtually unchanged after stability testing (Fig. S16). Additionally, the amount of O₂ product catalyzed by NiFeOOH electrode was collected at a constant current density of 1000 mA cm⁻² in 1 M KOH and determined via a water displacement method. As presented in Fig. S17, the Faradaic efficiency of NiFeOOH for OER is close to unity.

3.3. Detection of active metal sites

To gain insights on the underlying mechanism of the boosted OER intrinsic activity, the evolution of active metal sites and the corresponding interfacial interactions are systematically examined. In situ Raman spectroscopy is conducted to study the dynamics of Ni sites during reconstruction process. As depicted in Fig. S18, the signals of MoO₄²⁻ and Mo-O-Ni gradually decrease and disappear completely with increased bias voltage while two new Raman signals appeared at 1.50 and 1.45 V (vs. RHE) for NiMoO/FeB and NiMoO, respectively. The Raman shifts at 475 and 555 cm⁻¹ can be indexed to δ (Ni-O) and ν (Ni-O) modes, and correspond to γ and β phases in NiOOH, respectively (Fig. 4a-b) [33,47]. The corresponding potentials of these Raman peaks are consistent with those of anodic oxidation peaks in the first CV scanning curves of NiMoO/FeB and NiMoO (Fig. 4c), confirming the surface is dynamically reconstructed as NiOOH. Notably, the peak intensity labeled as $I_{\delta/\nu}$ determines the preferred β or γ NiOOH phase, where the higher $I_{\delta/\nu}$ corresponds to the active γ -NiOOH phase containing Ni⁴⁺ [19]. NiMoO/FeB exhibits higher $I_{\delta/\nu}$ values during the whole activation process (Fig. 4d), indicating that Ni²⁺ species are directly oxidized to Ni⁴⁺ species. Whereas NiMoO can only be oxidized to Ni³⁺ species at lower potentials [11]. According to potential-pH Pourbaix diagrams, deep oxidation of Ni²⁺ to Ni⁴⁺ is usually thermodynamically unfavorable and the Ni⁴⁺-containing phase is unstable in the resting state [8,22]. This explains why oxidation of NiMoO/FeB is completed at a higher potential (Fig. 4c). In addition, we observed that

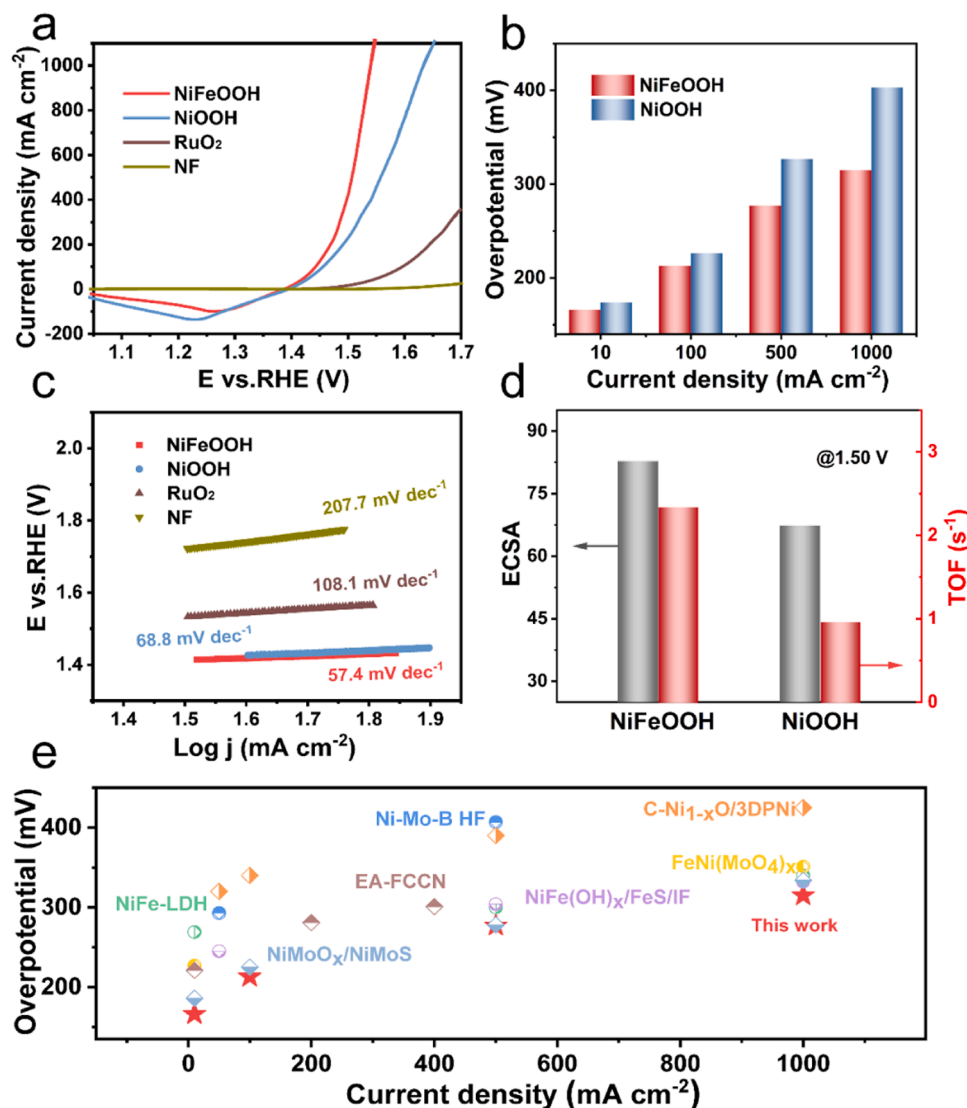


Fig. 3. (a) Reverse sweep LSV curves. (b) Overpotential comparisons of NiFeOOH and NiOOH. (c) Tafel slopes. (d) ECSA and TOF values of NiFeOOH and NiOOH at 1.50 V vs. RHE. (e) Overpotential comparisons with most recently reported electrocatalysts at different current densities.

FeOOH was formed at a lower potential (1.35 V) in NiMoO/FeB, and the Fe-O peak shifted with the increase of the potential (Fig. 4a). However, there is no distinct oxidation peak attributed to Fe in the CV curve, which could be attributed to an overlap between the oxidation peaks of Ni and Fe as well as the relatively low content of Fe in NiMoO/FeB [19]. According to the strong Lewis acidity of Fe³⁺, we hypothesized that the direct formation of Ni⁴⁺ is assisted by the formation of Fe-O-Ni motif, that conducts electron hopping from Ni to Fe, thereby stabilizing Ni⁴⁺ species [11,22]. Based on the EDS, ICP-OES, and *in situ* Raman spectroscopy results, it was deduced that there were two steps during the reconstruction process of NiMoO/FeB (Fig. S19). The surface B is initially oxidized and leached from NiMoO/FeB leaving behind a porous nanosheet structure, while Fe begins to oxidize at 1.35 V. Under the rising potential, the inner MoO₄²⁻ begins to leach and Fe-O-Ni motifs are formed as Ni and Fe ions migrate because of the strong induction effect of Fe³⁺ subsequently.

After electrochemical activation, the redox electrochemistry of Ni sites is investigated by CV scanning (Fig. S20). It can be seen that the oxidation of NiFeOOH is completed at a higher potential, verifying that the presence of Fe promotes direct deep oxidation to generate more tetravalent Ni [48]. Charge transfer kinetics is investigated by operando EIS at different potentials at high-frequency regions (5–10⁵ Hz), to

reflect the electron conductivity of the inner layer (Fig. S21) [49]. The charge transfer resistance of NiFeOOH was found to be stable after 1.50 V vs. RHE, whereas NiOOH was stable at a smaller potential (1.45 V), implying that NiOOH is oxidized at a lower potential with a limited deprotonation process, which is consistent with the CV results.

Raman spectroscopy was also employed to understand the resting state of metal sites (Fig. 4e). The higher $I_{\delta/\nu}$ value for NiFeOOH (2.69) implies that the local structure around Ni-O is different from NiOOH (1.55) due to the formation of more highly oxidized Ni⁴⁺ species during reconstruction process. Additionally, the peak around 1054 cm⁻¹ is ascribed to “active oxygen” species formed *via* deprotonation of nickel oxyhydroxide with peroxidic or superoxidic nature [22,38,39,50], providing direct evidence for the formation of NiO₂ species with tetravalent Ni. Core-level Ni 2p XPS spectra in Fig. S22 confirm the higher Ni oxidation state in NiFeOOH. And the Fe 2p peak at 712.0 eV indicates that Fe exists in the form of Fe³⁺ in NiFeOOH (Fig. S16d). The O 1s XPS spectra are deconvoluted into three peaks assigned to lattice oxygen (O1), oxygen atoms of surface hydroxyl groups (O2), and adsorbed water molecules (O3) (Fig. 4f). The O1 peak is shifted to 530.35 eV for NiFeOOH due to generation of the peroxo-like species (O₂²⁻) [51]. Moreover, the proportion of O₂²⁻ increases significantly coupled with the decrease of OH⁻ species, indicating a higher amount of NiO₂ in NiFeOOH

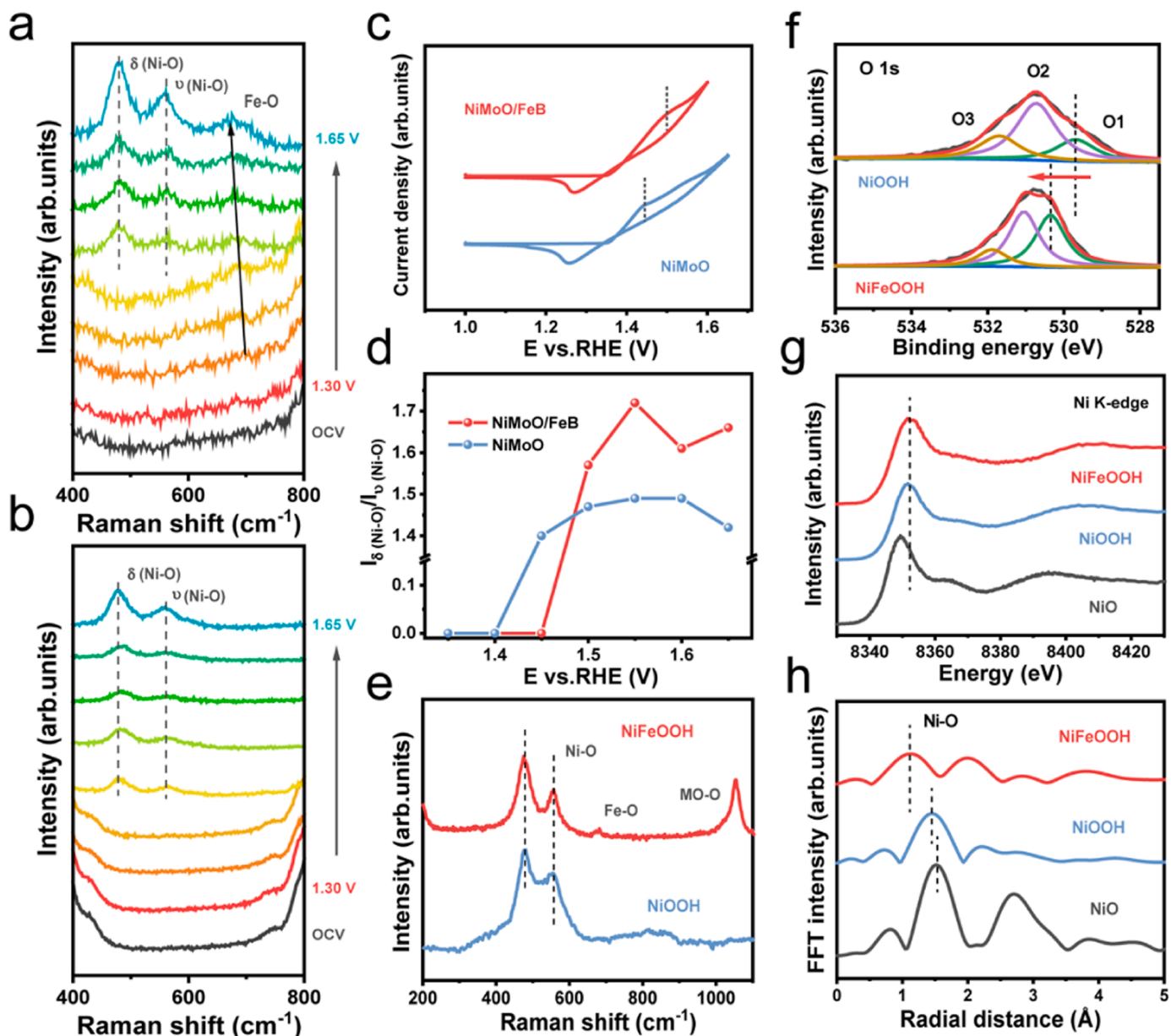


Fig. 4. Operando Raman spectra of (a) NiMoO/FeB and (b) NiMoO at the operated potentials from 1.30 to 1.65 V vs. RHE. (c) First CV scanning curves and (d) I_{δ}/I_{ν} in operando Raman spectra of NiMoO and NiMoO/FeB. (e) Raman spectra, (f) O 1s XPS spectra, (g) Ni K-edge XANES and (h) EXAFS of NiOOH and NiFeOOH.

than in NiOOH (Table S5).

The Ni electronic states are also substantiated by Ni K-edge X-ray absorption near edge structure (XANES) spectroscopy. The white line peak, related to the $1s$ to $4p$ transition, peaked at 8352.66 eV in the XANES spectrum of NiFeOOH, higher than that of NiOOH (Fig. 4g). This indicates that the average oxidation state of Ni in NiFeOOH is higher than that in NiOOH, and suggests the formation of more Ni^{4+} species in NiFeOOH [51,52]. Meanwhile, the shift to lower energy, peak broadening and the increased intensity of the edge transitions (i.e., $1s \rightarrow 4p$), which are sensitive to ligand-metal covalency, occur for NiFeOOH due to the delocalization of the metal $4p$ orbitals and signify the increased Ni-O covalency (Fig. S23) [22].

The Fast Fourier-transformed (FFT) extended X-ray absorption fine structure (EXAFS) $k^3\chi$ data of the Ni K-edge are further calculated to examine the local atomic structure (Fig. 4h and Fig. S24). The interatomic distance of Ni-O scattering path for NiFeOOH decreases from 1.98 to 1.85 Å compared to NiOOH (Table S6), verifying the increase of covalency of Ni-O bond. The shift in Ni-O scattering path is attributed

to the different local coordination environments in NiOOH and NiFeOOH because of the different proportions of NiOOH and NiO_2 phases [51].

The above observations suggest that the predominant resting state of NiFeOOH is Fe-doped NiO_2 species, caused by Fe doping and the reconstruction process (i.e., electrochemical polarization at moderately high potentials). The increased Ni^{4+} generation leads to greater Ni-O covalency, which facilitates the activation of lattice oxygen [14,39].

3.4. Research on the reaction pathway

The higher oxidation state of Ni active sites and the active oxygen species provide indirect evidence for LOM pathway during OER. Also, the pH-dependent OER measurements demonstrate a more appreciable enhancement in the current density delivered by NiFeOOH with increasing alkalinity compared with NiOOH (Fig. S25). The linear relationship between current density and pH at 1.55 V (vs. RHE) determines the proton reaction order ($\rho^{\text{RHE}} = \partial \log i / \partial \text{pH}$) (Fig. 5a).

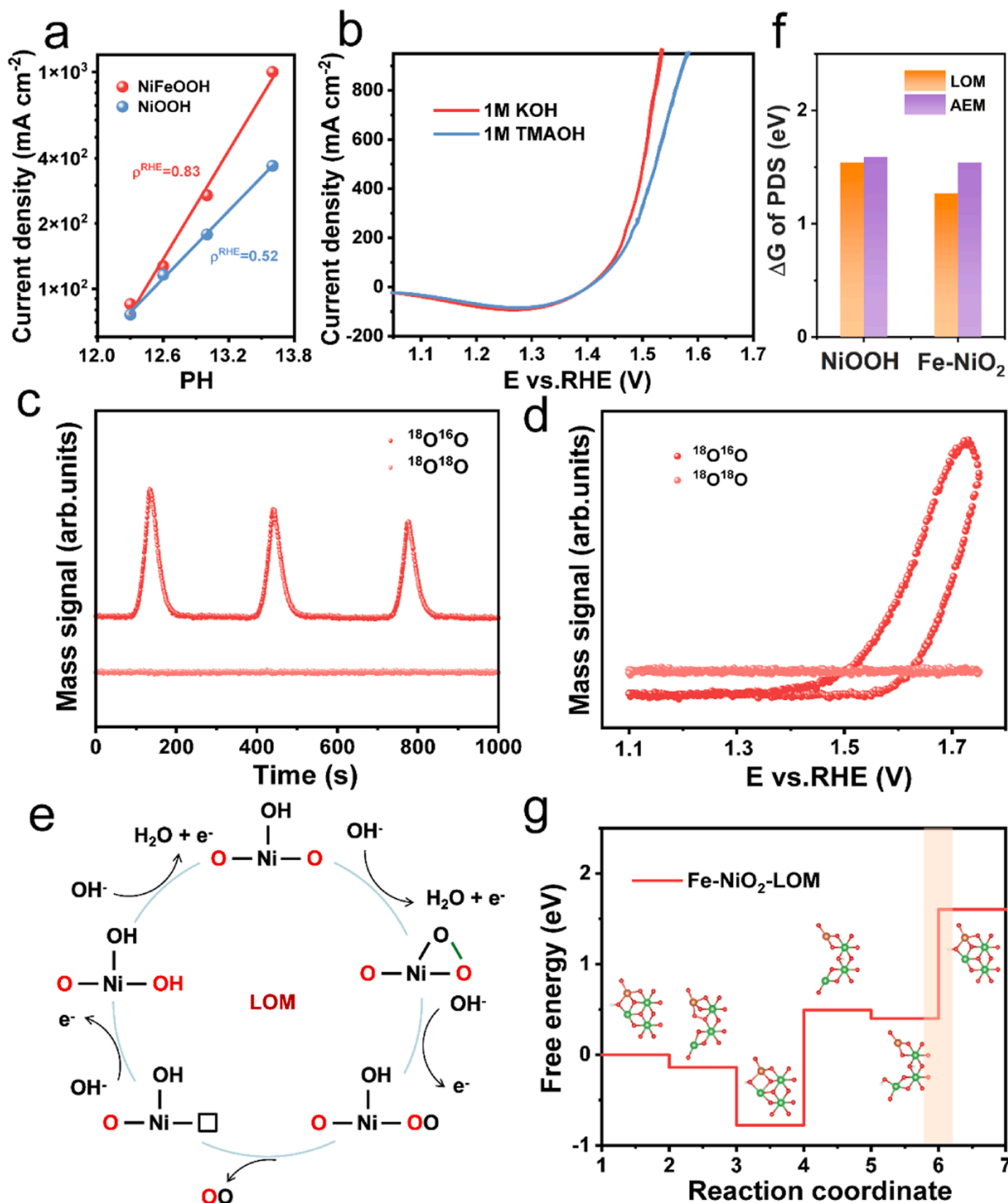


Fig. 5. (a) The OER current densities of NiOOH and NiFeOOH at 1.55 V vs. RHE under different pH values. (b) Reverse sweep LSV curves for NiFeOOH measured in 1 M KOH and 1 M TMAOH. (c) The DEMS signals of $^{34}\text{O}_2$ and $^{36}\text{O}_2$ vs. time for NiFeOOH. (d) The DEMS signals of $^{34}\text{O}_2$ and $^{36}\text{O}_2$ vs. applied potential for NiFeOOH. (e) Schematic illustration of LOM pathway. (f) The energy barrier of PDS via LOM and AEM pathways in different models. (g) Gibbs free energy diagrams of LOM pathway on Fe-NiO₂ model (Ni, Fe and O are shown in green, yellow and red, respectively).

NiFeOOH exhibits a higher j^{RHE} (0.83) than NiOOH (0.52), implying a stronger pH dependence of OER activity for NiFeOOH [13,53–55], along with a higher degree of non-concerted proton/electron transfer process such as lattice oxygen oxidation [56]. As surface superoxide intermediates are critical to LOM mechanism, tetramethylammonium hydroxide (TMAOH) is used to probe the presence of lattice oxygen catalyzing OER [13]. As shown in Fig. 5b, the OER activity of NiFeOOH dramatically decreased in TMAOH-containing solution, alluding to the restraint of water oxidation owing to the strong bonding of TMA^+ cation with surface superoxide intermediates. In comparison, TMA^+ cation has an inconspicuous influence on the OER activity of NiOOH (Fig. S26). Both higher proton reaction order and debilitated performance by the addition of TMAOH suggest that NiFeOOH follows LOM pathway instead of the conventional AEM pathway during OER process.

To directly verify the involvement of lattice oxygen in water oxidation, ^{18}O isotope labeling and *in situ* DEMS experiments were performed [10,57]. As shown in Fig. 5c, the DEMS results on the ^{18}O -labeled NiFeOOH showed a significant periodic signal of $^{18}\text{O}^{16}\text{O}$ ($m/z = 34$) confirming that the lattice oxygen participated in OER. Although the periodic $^{34}\text{O}_2$ evolution was also observed on ^{18}O -labeled NiOOH, the much lower signal intensity manifests NiFeOOH with tetravalent Ni is more conducive to the lattice oxygen activation (Fig. S27). Furthermore, the mass spectrometry cyclic voltammograms (MSCVs) can directly compare the participation of lattice oxygen in the OER process [55]. The absent $^{18}\text{O}^{18}\text{O}$ ($m/z = 36$) signal in Fig. 5d indicates that the OER pathway follows a single-metal-site mechanism rather than a dual-metal-site mechanism on NiFeOOH. That is to say, the formed O_2 molecule comes from the direct coupling of the $^*\text{O}$ intermediate and activated lattice oxygen instead of the intramolecular oxygen coupling of adjacent activated lattice oxygen [10].

Finally, DFT calculations are conducted to verify the effect of Fe-O-Ni motif on the formation of Ni^{4+} and comprehend the reasons for improved performance at NiFeOOH. As shown in Fig. S28, based on experimental results and previous literature reports [58], we constructed NiOOH and Fe-NiOOH models with interlayer H_2O and K^+ , and found that Fe-NiOOH is more likely to deproton to form Fe-NiO₂ during electrooxidation due to the presence of Fe-O-Ni motif (Fig. S29). Therefore, slab models of NiOOH and Fe-NiO₂ were used to represent NiOOH and NiFeOOH in this work to further investigate the OER pathway (Fig. 5e, Fig. S30 and Table S7). As depicted in Fig. 5f, the predicted energy barrier manifests that Fe-NiO₂ holds a lower value than NiOOH through both AEM and LOM pathways. Also, the LOM pathway is more energetically favorable on Fe-NiO₂ model, confirming that NiFeOOH favors lattice oxygen evolution. In the AEM pathway (Fig. S31), the $^*\text{O} \rightarrow ^*\text{OOH}$ is identified as the potential determining step (PDS) for NiOOH. Whereas the PDS is transferred to the deprotonation of $^*\text{OOH}$ for Fe-NiO₂, indicating that the electronic modulation alters the chemical affinity of OER intermediates to reduce the energy barrier and improve the OER activity. In the LOM pathway, the coupling of O-O with a high potential barrier of 1.54 eV served as the PDS for NiOOH (Fig. S32). Whereas the PDS shifts to the deprotonation of $^*\text{OH}$ on Fe-NiO₂ with a diminished potential barrier of 1.27 eV, which is consistent with the pH-dependent measurements results (Fig. 5g). Furthermore, in order to explain the mechanism of lattice oxygen activation, the Ni 3d and O 2p bands of NiOOH and Fe-NiO₂ are analyzed. As shown in Fig. S33, the overlap of Ni 3d and O 2p orbitals in Fe-NiO₂ increases significantly, indicating the enhancement of Ni-O covalency, which is consistent with the XAS results. In addition, due to the formation of Ni^{4+} , the LHB band of Ni moves down and the O 2p band upshift, which significantly increases U and reduces Δ , thus activating lattice oxygen and reducing the reaction energy barrier of Fe-NiO₂ (Table S8). In summary, both experimental and simulation results indicate that optimal Fe doping and electrooxidation at medium/high potentials boost the formation and stabilization of tetravalent Ni and active oxygen species, thereby enhancing the covalency of Ni-O, transferring PDS into a pH-dependent deprotonation step, and ultimately

providing superior OER performance.

4. Conclusions

The reconstruction of NiMoO/FeB is reported to form NiFeOOH nanosheets/rods structure with stable tetravalent Ni species as a high-efficiency OER electrocatalyst. The formation and stabilization of tetravalent Ni and active oxygen species due to the formation of Fe-O-Ni motifs, offer stronger Ni-O covalency and reduce the reaction energy barrier by activating lattice oxygen. The resulting NiFeOOH exhibits extraordinary OER activity, only 166 and 315 mV are required to achieve 10 and 1000 mA cm^{-2} , respectively. Combined with the incorporation of B, the formed 3D nanosheets/rods structure enables stable water oxidation at 1000 mA cm^{-2} for over 100 h. This work proves that the electronic structure and morphology of the reconstructed catalysts can be efficiently modulated via introducing metal/non-metal ions into the pre-catalysts. This strategy can be popularized to other TM materials, including but not limited to introducing metal Fe, Cu, Mn, V and non-metallic P, S, Se, F into other Ni/Co-based pre-catalysts for water oxidation reactions and a range of electrochemical energy applications beyond.

CRediT authorship contribution statement

Yijie Zhang: Conceptualization, Methodology, Data curation, Writing –original draft preparation. **Kamran Dastafkan:** Writing – review & editing, Data curation. **Qiang Zhao:** Supervision, Project administration. **Jinping Li:** Supervision, Project administration. **Chuan Zhao:** Visualization, Investigation, Project administration, Funding acquisition. **Guang Liu:** Writing – review & editing, Project administration, Funding acquisition.

Declaration of Competing Interest

The authors declare that they have no known competing financial interests or personal relationships that could have appeared to influence the work reported in this paper.

Data Availability

Data will be made available on request.

Acknowledgments

This work was supported by the National Natural Science Foundation of China (No. 22075196, U22A20418, 21878204) and the Key Research and Development Program of Shanxi Province (No.201903D421073), Research Project Supported by Shanxi Scholarship Council of China (2022-050). C.Z. and K.D acknowledge the support from Australian Research Council (IC200100023, DP220103294, CE230100017).

Appendix A. Supporting information

Supplementary data associated with this article can be found in the online version at doi:10.1016/j.apcatb.2023.123297.

References

- [1] Z.W. Seh, J. Kibsgaard, C.F. Dickens, I.B. Chorkendorff, J.K. Nørskov, T. F. Jaramillo, Combining theory and experiment in electrocatalysis: insights into materials design, *Science* 355 (2017), eaad4998, <https://doi.org/10.1126/science.aad4998>.
- [2] C.G. Morales-Guio, L.-A. Stern, X. Hu, Nanostructured hydrotreating catalysts for electrochemical hydrogen evolution, *Chem. Soc. Rev.* 43 (2014) 6555–6569, <https://doi.org/10.1039/C3CS60468C>.
- [3] Z. Li, X. Xu, X. Lu, C. He, J. Huang, W. Sun, L. Tian, Synergistic coupling of FeNi₃ alloy with graphene carbon dots for advanced oxygen evolution reaction

- electrocatalysis, *J. Colloid Interface Sci.* 615 (2022) 273–281, <https://doi.org/10.1016/j.jcis.2022.01.088>.
- [4] F. Chang, M. Xiao, R. Miao, Y. Liu, M. Ren, Z. Jia, D. Han, Y. Yuan, Z. Bai, L. Yang, Copper-based catalysts for electrochemical carbon dioxide reduction to multicarbon products, *Electrochem. Energy Rev.* 5 (2022), 4, <https://doi.org/10.1007/s41918-022-00139-5>.
 - [5] Q. Che, Q. Li, X. Chen, Y. Tan, X. Xu, Assembling amorphous (Fe-Ni)Co-OH/Ni₃S₂ nanohybrids with S-vacancy and interfacial effects as an ultra-highly efficient electrocatalyst: Inner investigation of mechanism for alkaline water-to-hydrogen/oxygen conversion, *Appl. Catal., B* 263 (2020), 118338, <https://doi.org/10.1016/j.apcatb.2019.118338>.
 - [6] L.J.J. Janssen, S.J.D.V. Stralen, Bubble behaviour on and mass transfer to an oxygen-evolving transparent nickel electrode in alkaline solution, *Electrochim. Acta* 26 (1981) 1011–1022, [https://doi.org/10.1016/0013-4686\(81\)85070-0](https://doi.org/10.1016/0013-4686(81)85070-0).
 - [7] C. Zhang, F. Wang, M. Batool, B. Xiong, H. Yang, Phase transition of SrCo_{0.9}Fe_{0.1}O₃ electrocatalysts and their effects on oxygen evolution reaction, *SusMat* 2 (2022) 445–455, <https://doi.org/10.1002/sus2.72>.
 - [8] X. Zheng, B. Zhang, P. De Luna, Y. Liang, R. Comin, O. Voznyy, L. Han, F.P. García de Arquer, M. Liu, C.T. Dinh, T. Regier, J.J. Dynes, S. He, H.L. Xin, H. Peng, D. Prendergast, X. Du, E.H. Sargent, Theory-driven design of high-valence metal sites for water oxidation confirmed using in situ soft X-ray absorption, *Nat. Chem.* 10 (2018) 149–154, <https://doi.org/10.1038/nchem.2886>.
 - [9] D.K. Bediako, B. Lassalle-Kaiser, Y. Surendranath, J. Yano, V.K. Yachandra, D. G. Nocera, Structure–activity correlations in a nickel–borate oxygen evolution catalyst, *J. Am. Chem. Soc.* 134 (2012) 6801–6809, <https://doi.org/10.1021/ja301018q>.
 - [10] N. Zhang, Y. Chai, Lattice oxygen redox chemistry in solid-state electrocatalysts for water oxidation, *Energy Environ. Sci.* 14 (2021) 4647–4671, <https://doi.org/10.1039/D1EE01277K>.
 - [11] N. Zhang, X. Feng, D. Rao, X. Deng, L. Cai, B. Qiu, R. Long, Y. Xiong, Y. Lu, Y. Chai, Lattice oxygen activation enabled by high-valence metal sites for enhanced water oxidation, *Nat. Commun.* 11 (2020), 4066, <https://doi.org/10.1038/s41467-020-17934-7>.
 - [12] J.J. Song, C. Wei, Z.F. Huang, C.T. Liu, L. Zeng, X. Wang, Z.C. Xu, A review on fundamentals for designing oxygen evolution electrocatalysts, *Chem. Soc. Rev.* 49 (2020) 2196–2214, <https://doi.org/10.1039/c9cs00607a>.
 - [13] Y. Wu, Y. Zhao, P. Zhai, C. Wang, J. Gao, L. Sun, J. Hou, Triggering lattice oxygen activation of single-atomic mo sites anchored on ni-fe oxyhydroxides nanoarrays for electrochemical water oxidation, *Adv. Mater.* 34 (2022), 2202523, <https://doi.org/10.1002/adma.202202523>.
 - [14] Z.-F. Huang, J. Song, Y. Du, S. Xi, S. Dou, J.M.V. Nsanzimana, C. Wang, Z.J. Xu, X. Wang, Chemical and structural origin of lattice oxygen oxidation in Co–Zn oxyhydroxide oxygen evolution electrocatalysts, *Nat. Energy* 4 (2019) 329–338, <https://doi.org/10.1038/s41560-019-0355-9>.
 - [15] M. Bajdich, M. García-Mota, A. Vojvodic, J.K. Nørskov, A.T. Bell, Theoretical investigation of the activity of cobalt oxides for the electrochemical oxidation of water, *J. Am. Chem. Soc.* 135 (2013) 13521–13530, <https://doi.org/10.1021/ja405997s>.
 - [16] M. Chatenet, B.G. Pollet, D.R. Dekel, F. Dionigi, J. Deseure, P. Millet, R.D. Braatz, M.Z. Bazant, M. Eikerling, I. Staffell, P. Balcombe, Y. Shao-Horn, H. Schäfer, Water electrolysis: from textbook knowledge to the latest scientific strategies and industrial developments, *Chem. Soc. Rev.* 51 (2022) 4583–4762, <https://doi.org/10.1039/D0CS01079K>.
 - [17] J. Chen, H. Chen, T. Yu, R. Li, Y. Wang, Z. Shao, S. Song, Recent advances in the understanding of the surface reconstruction of oxygen evolution electrocatalysts and materials development, *Electrochem. Energy Rev.* 4 (2021) 566–600, <https://doi.org/10.1007/s41918-021-00104-8>.
 - [18] J. Zhang, Y. Ye, B. Wei, F. Hu, L. Sui, H. Xiao, L. Gui, J. Sun, B. He, L. Zhao, Unveiling anion induced surface reconstruction of perovskite oxide for efficient water oxidation, *Appl. Catal., B* 330 (2023), 122661, <https://doi.org/10.1016/j.apcatb.2023.122661>.
 - [19] H. Lei, L. Ma, Q. Wan, S. Tan, B. Yang, Z. Wang, W. Mai, H.J. Fan, Promoting surface reconstruction of NiFe layered double hydroxide for enhanced oxygen evolution, *Adv. Energy Mater.* 12 (2022), 2202522, <https://doi.org/10.1002/aenm.202202522>.
 - [20] S. Ye, Y. Lei, T. Xu, L. Zheng, Z. Chen, X. Yang, X. Ren, Y. Li, Q. Zhang, J. Liu, Deeply self-reconstructing CoFe(H₃O)(PO₄)₂ to low-crystalline Fe_{0.5}Co_{0.5}OOH with Fe³⁺–O–Fe³⁺ motifs for oxygen evolution reaction, *Appl. Catal., B* 304 (2022), 120986, <https://doi.org/10.1016/j.apcatb.2021.120986>.
 - [21] J.-Y. Luo, Y. Yuan, H.-Y. Ruan, X.-Q. Wu, Y.-P. Wu, S. Li, G. Zhang, S. Sun, D.-S. Li, Electrochemical reconstruction engineering: metal–organic gels as pre-catalysts for NiOOH/FeOOH heterostructure to boost oxygen evolution reaction, *Small Struct.* (2023), 2300074, <https://doi.org/10.1002/ssr.202300074>.
 - [22] N. Li, D.K. Bediako, R.G. Hadt, D. Hayes, T.J. Kempa, F. Von Cube, D.C. Bell, L. X. Chen, D.G. Nocera, Influence of iron doping on tetraavalent nickel content in catalytic oxygen evolving films, *PNAS* 114 (2017) 1486–1491, <https://doi.org/10.1073/pnas.1620787114>.
 - [23] H. Liu, X. Li, L. Chen, X. Zhu, P. Dong, M.O.L. Chee, M. Ye, Y. Guo, J. Shen, Monolithic Ni–Mo–B bifunctional electrode for large current water splitting, *Adv. Funct. Mater.* 32 (2022), 2107308, <https://doi.org/10.1002/adfm.202107308>.
 - [24] T.Y. Kou, S.W. Wang, R.P. Shi, T. Zhang, S. Chiovoloni, J.Q. Lu, W. Chen, M. A. Worsley, B.C. Wood, S.E. Baker, E.B. Duoss, R. Wu, C. Zhu, Y. Li, Periodic porous 3D electrodes mitigate gas bubble traffic during alkaline water electrolysis at high current densities, *Adv. Energy Mater.* 10 (2020), 2002955, <https://doi.org/10.1002/aenm.202002955>.
 - [25] P. Wang, Y. Luo, G. Zhang, Z. Chen, H. Ranganathan, S. Sun, Z. Shi, Interface engineering of Ni₂S₃@MnOxHy nanorods to efficiently enhance overall-water-splitting activity and stability, *Nano-Micro Lett.* 14 (2022), 120, <https://doi.org/10.1007/s40820-022-00860-2>.
 - [26] H.-Y. Jeong, J. Oh, G.S. Yi, H.-Y. Park, S.K. Cho, J.H. Jang, S.J. Yoo, H.S. Park, High-performance water electrolyzer with minimum platinum group metal usage: Iron nitride–iridium oxide core–shell nanostructures for stable and efficient oxygen evolution reaction, *Appl. Catal., B* 330 (2023), 122596, <https://doi.org/10.1016/j.apcatb.2023.122596>.
 - [27] Y. Zhang, R. Yao, Y. Wu, Q. Zhao, J. Li, G. Liu, In situ rapid and deep self-reconstruction of Fe-doped hydrate NiMoO₄ for stable water oxidation at high current densities, *Chem. Eng. J.* 461 (2023), 142081, <https://doi.org/10.1016/j.cej.2023.142081>.
 - [28] K. Eda, Y. Kato, Y. Ohshiro, T. Sugitani, M.S. Whittingham, Synthesis, crystal structure, and structural conversion of Ni molybdate hydrate NiMoO₄·nH₂O, *J. Solid State Chem.* 183 (2010) 1334–1339, <https://doi.org/10.1016/j.jssc.2010.04.009>.
 - [29] K. Eda, Y. Uno, N. Nagai, N. Sotani, M. Stanley Whittingham, Crystal structure of cobalt molybdate hydrate CoMoO₄·nH₂O, *J. Solid State Chem.* 178 (2005) 2791–2797, <https://doi.org/10.1016/j.jssc.2005.06.014>.
 - [30] G. Solomon, A. Landström, R. Mazzaro, M. Jugovac, P. Moras, E. Cattaruzza, V. Morandi, I. Concina, A. Vomiero, NiMoO₄@Co₃O₄ core–shell nanorods: in situ catalyst reconstruction toward high efficiency oxygen evolution reaction, *Adv. Energy Mater.* 11 (2021), 2101324, <https://doi.org/10.1002/aenm.202101324>.
 - [31] X. Liu, J. Meng, K. Ni, R. Guo, F. Xia, J. Xie, X. Li, B. Wen, P. Wu, M. Li, J. Wu, X. Wu, L. Mai, D. Zhao, Complete reconstruction of hydrate pre-catalysts for ultrastable water electrolysis in industrial-concentration alkali media, *Cell Rep. Phys. Sci.* 1 (2020), 100241, <https://doi.org/10.1016/j.xcrp.2020.100241>.
 - [32] Y. Wang, Y.L. Zhu, S.L. Zhao, S.X. She, F.F. Zhang, Y. Chen, T. Williams, T. Gengenbach, L.H. Zu, H.Y. Mao, W. Zhou, Z.P. Shao, H.T. Wang, J. Tang, D. Y. Zhao, C. Selomulya, Anion etching for accessing rapid and deep self-reconstruction of precatalysts for water oxidation, *Matter* 3 (2020) 2124–2137, <https://doi.org/10.1016/j.matt.2020.09.016>.
 - [33] K. Dastafkan, S. Wang, C. Rong, Q. Meyer, Y. Li, Q. Zhang, C. Zhao, Cosynergistic molybdate oxo-anionic modification of FeNi-based electrocatalysts for efficient oxygen evolution reaction, *Adv. Funct. Mater.* 32 (2022), 2107342, <https://doi.org/10.1002/adfm.202107342>.
 - [34] J.M.V. Nsanzimana, R. Dangol, V. Reddu, S. Duo, Y. Peng, K.N. Dinh, Z. Huang, Q. Yan, X. Wang, Facile synthesis of amorphous ternary metal borides–reduced graphene oxide hybrid with superior oxygen evolution activity, *ACS Appl. Mater. Interfaces* 11 (2019) 846–855, <https://doi.org/10.1021/acsami.8b17836>.
 - [35] N. Wang, A. Xu, P. Ou, S.-F. Hung, A. Ozden, Y.-R. Lu, J. Abed, Z. Wang, Y. Yan, M.-J. Sun, Y. Xia, M. Han, J. Han, K. Yao, F.-Y. Wu, P.-H. Chen, A. Vomiero, A. Seifitokaldani, X. Sun, D. Sinton, Y. Liu, E.H. Sargent, H. Liang, Boride-derived oxygen-evolution catalysts, *Nat. Commun.* 12 (2021), 6089, <https://doi.org/10.1038/s41467-021-26307-7>.
 - [36] J. Li, H. Chen, Y. Liu, R. Gao, X. Zou, In situ structural evolution of a nickel boride catalyst: synergistic geometric and electronic optimization for the oxygen evolution reaction, *J. Mater. Chem. A* 7 (2019) 5288–5294, <https://doi.org/10.1039/C9TA00489K>.
 - [37] F. Guo, Y. Wu, H. Chen, Y. Liu, L. Yang, X. Ai, X. Zou, High-performance oxygen evolution electrocatalysis by boronized metal sheets with self-functionalized surfaces, *Energy Environ. Sci.* 12 (2019) 684–692, <https://doi.org/10.1039/C8EE03405B>.
 - [38] S. Lee, K. Banjac, M. Lingenfelder, X. Hu, Oxygen isotope labeling experiments reveal different reaction sites for the oxygen evolution reaction on nickel and nickel iron oxides, *Angew. Chem. Int. Ed.* 58 (2019) 10295–10299, <https://doi.org/10.1002/anie.201903200>.
 - [39] B.J. Trześniewski, O. Diaz-Morales, D.A. Vermaas, A. Longo, W. Bras, M.T. M. Koper, W.A. Smith, In situ observation of active oxygen species in Fe-containing Ni-based oxygen evolution catalysts: the effect of pH on electrochemical activity, *J. Am. Chem. Soc.* 137 (2015) 15112–15121, <https://doi.org/10.1021/jacs.5b06814>.
 - [40] X. Zou, Y.P. Liu, G.D. Li, Y.Y. Wu, D.P. Liu, W. Li, H.W. Li, D.J. Wang, Y. Zhang, X. Zou, Ultrafast formation of amorphous bimetallic hydroxide films on 3d conductive sulfide nanoarrays for large-current-density oxygen evolution electrocatalysis, *Adv. Mater.* 29 (2017), 1700404, <https://doi.org/10.1002/adma.201700404>.
 - [41] P. Zhai, Y. Zhang, Y. Wu, J. Gao, B. Zhang, S. Cao, Y. Zhang, Z. Li, L. Sun, J. Hou, Engineering active sites on hierarchical transition bimetal oxides/sulfides heterostructure array enabling robust overall water splitting, *Nat. Commun.* 11 (2020), 5462, <https://doi.org/10.1038/s41467-020-19214-w>.
 - [42] X. Yu, Z.Y. Yu, X.L. Zhang, Y.R. Zheng, Y. Duan, Q. Gao, R. Wu, B. Sun, M.R. Gao, G. Wang, S.H. Yu, “Superaerophobic” nickel phosphide nanoarray catalyst for efficient hydrogen evolution at ultrahigh current densities, *J. Am. Chem. Soc.* 141 (2019) 7537–7543, <https://doi.org/10.1021/jacs.9b02527>.
 - [43] Y. Zhao, J. Zhang, Y. Xie, B. Sun, J. Jiang, W.-J. Jiang, S. Xi, H.Y. Yang, K. Yan, S. Wang, X. Guo, P. Li, Z. Han, X. Lu, H. Liu, G. Wang, Constructing atomic heterometallic sites in ultrathin nickel-incorporated cobalt phosphide nanosheets via a boron-assisted strategy for highly efficient water splitting, *Nano Lett.* 21 (2021) 823–832, <https://doi.org/10.1021/acs.nanolett.0c04569>.
 - [44] Y. Zhang, L. Liu, J. Wang, R. Yao, Y. Wu, M. Wang, Q. Zhao, J. Li, G. Liu, Rational introduction of S and P in multi-stage electrocatalyst to drive a large-current-density water oxidation reaction and overall water splitting, *J. Power Sources* 518 (2022), 230757, <https://doi.org/10.1016/j.jpowsour.2021.230757>.

- [45] Y.P. Liu, X. Liang, L. Gu, Y. Zhang, G.D. Li, X.X. Zou, J.S. Chen, Corrosion engineering towards efficient oxygen evolution electrodes with stable catalytic activity for over 6000 h, *Nat. Commun.* 9 (2018) 2609–2619, <https://doi.org/10.1038/s41467-018-05019-5>.
- [46] S. Niu, W.J. Jiang, T. Tang, L.P. Yuan, H. Luo, J.S. Hu, Autogenous Growth of Hierarchical NiFe(OH)_x/FeS Nanosheet-On-Microsheet Arrays for Synergistically Enhanced High-Output Water Oxidation, *Adv. Funct. Mater.* 29 (2019) 1902180–1902189, <https://doi.org/10.1002/adfm.201902180>.
- [47] X. Bo, R.K. Hocking, S. Zhou, Y. Li, X. Chen, J. Zhuang, Y. Du, C. Zhao, Capturing the active sites of multimetallic (oxy)hydroxides for the oxygen evolution reaction, *Energy Environ. Sci.* 13 (2020) 4225–4237, <https://doi.org/10.1039/D0EE01609H>.
- [48] T. Wu, S. Sun, J. Song, S. Xi, Y. Du, B. Chen, W.A. Sasangka, H. Liao, C.L. Gan, G. G. Scherer, L. Zeng, H. Wang, H. Li, A. Grimaud, Z.J. Xu, Iron-facilitated dynamic active-site generation on spinel CoAl₂O₄ with self-termination of surface reconstruction for water oxidation, *Nat. Catal.* 2 (2019) 763–772, <https://doi.org/10.1038/s41929-019-0325-4>.
- [49] X. Chen, Q. Wang, Y. Cheng, H. Xing, J. Li, X. Zhu, L. Ma, Y. Li, D. Liu, S-doping triggers redox reactivities of both iron and lattice oxygen in FeOOH for low-cost and high-performance water oxidation, *Adv. Funct. Mater.* 32 (2022), 2112674, <https://doi.org/10.1002/adfm.202112674>.
- [50] C. Hu, Y. Hu, C. Fan, L. Yang, Y. Zhang, H. Li, W. Xie, Surface-enhanced raman spectroscopic evidence of key intermediate species and role of NiFe dual-catalytic center in water oxidation, *Angew. Chem. Int. Ed.* 60 (2021) 19774–19778, <https://doi.org/10.1002/anie.202103888>.
- [51] A. Moysiadou, S. Lee, C.-S. Hsu, H.M. Chen, X. Hu, Mechanism of oxygen evolution catalyzed by cobalt oxyhydroxide: cobalt superoxide species as a key intermediate and dioxygen release as a rate-determining step, *J. Am. Chem. Soc.* 142 (2020) 11901–11914, <https://doi.org/10.1021/jacs.0c04867>.
- [52] W.H. Lee, M.H. Han, Y.-J. Ko, B.K. Min, K.H. Chae, H.-S. Oh, Electrode reconstruction strategy for oxygen evolution reaction: maintaining Fe-CoOOH phase with intermediate-spin state during electrolysis, *Nat. Commun.* 13 (2022), 605, <https://doi.org/10.1038/s41467-022-28260-5>.
- [53] Y. Pan, X. Xu, Y. Zhong, L. Ge, Y. Chen, J.-P.M. Veder, D. Guan, R. O'hayre, M. Li, G. Wang, H. Wang, W. Zhou, Z. Shao, Direct evidence of boosted oxygen evolution over perovskite by enhanced lattice oxygen participation, *Nat. Commun.* 11 (2020), 2002, <https://doi.org/10.1038/s41467-020-15873-x>.
- [54] Y. Zhu, Z. He, Y. Choi, H. Chen, X. Li, B. Zhao, Y. Yu, H. Zhang, K.A. Stoerzinger, Z. Feng, Y. Chen, M. Liu, Tuning proton-coupled electron transfer by crystal orientation for efficient water oxidization on double perovskite oxides, *Nat. Commun.* 11 (2020), 4299, <https://doi.org/10.1038/s41467-020-17657-9>.
- [55] Z. He, J. Zhang, Z. Gong, H. Lei, D. Zhou, N. Zhang, W. Mai, S. Zhao, Y. Chen, Activating lattice oxygen in NiFe-based (oxy)hydroxide for water electrolysis, *Nat. Commun.* 13 (2022), 2191, <https://doi.org/10.1038/s41467-022-29875-4>.
- [56] A. Grimaud, O. Diaz-Morales, B. Han, W.T. Hong, Y.-L. Lee, L. Giordano, K. A. Stoerzinger, M.T.M. Koper, Y. Shao-Horn, Activating lattice oxygen redox reactions in metal oxides to catalyse oxygen evolution, *Nat. Chem.* 9 (2017) 457–465, <https://doi.org/10.1038/nchem.269>.
- [57] C. Wang, P. Zhai, M. Xia, W. Liu, J. Gao, L. Sun, J. Hou, Identification of the origin for reconstructed active sites on oxyhydroxide for oxygen evolution reaction, *Adv. Mater.* 35 (2023), 2209307, <https://doi.org/10.1002/adma.202209307>.
- [58] F. Dionigi, Z. Zeng, I. Sinev, T. Merzdorf, S. Deshpande, M.B. Lopez, S. Kunze, I. Zegkinoglou, H. Sarodnik, D. Fan, A. Bergmann, J. Drnec, J.F.D. Araujo, M. Gliech, D. Teschner, J. Zhu, W.-X. Li, J. Greeley, B.R. Cuenya, P. Strasser, In-situ structure and catalytic mechanism of NiFe and CoFe layered double hydroxides during oxygen evolution, *Nat. Commun.* 11 (2020), 2522, <https://doi.org/10.1038/s41467-020-16237-1>.